

**SYNTHESIS AND CHARACTERISATION OF
ELECTROSPUN DOPED TIN(IV) OXIDE/
POLYANILINE/POLYHYDROXYBUTYRATE
NANOCOMPOSITE FOR ETHANOL GAS
SENSOR**

VICINISVARRI A/P INDERAN

UNIVERSITI SAINS MALAYSIA

2019

**SYNTHESIS AND CHARACTERISATION OF
ELECTROSPUN DOPED TIN(IV) OXIDE/
POLYANILINE/POLYHYDROXYBUTYRATE
NANOCOMPOSITE FOR ETHANOL GAS
SENSOR**

by

VICINISVARRI A/P INDERAN

**Thesis submitted in fulfilment of the requirements
for the degree of
Doctor of Philosophy**

August 2019

ACKNOWLEDGEMENT

First and foremost, I'm grateful to The Almighty God for His blessings and graces. My sincere gratitude to my supervisor Dr. Lee Hooi Ling and my co-supervisor Prof. Sudesh Kumar, without them this work would not have been possible. Thank you so much for the continuous guidance and assistance throughout this project. I also gratefully acknowledge the Minister of Higher Education (MoHE), Malaysia for financial assistance provided for this research under the Skim Latihan Akademik IPTA (SLAI) and Fundamental Research Grant Scheme (203/PKIMIA/6711363).

I also would like to thank all our research collaborators: Prof. Dr. A.s. Md. Abdul Haseeb and Dr. M. M. Arafat (University of Malaya) for the gas sensor system facility, Prof. Satoshi Ichikawa (Osaka University, Japan), Nadi Braidy and Samuel Bastian (Université de Sherbrooke) for valuable advices on the HRTEM, SAED and XRD results.

Special thanks to all my friends for helping me with this project, especially Shin Ye Lim, Shaik Ling Ang, Sunderishwary, Nur Ruzaina Rahman, Murugan and all the staff of School of Chemical Sciences for providing the facilities, knowledge and assistance.

My appreciation also goes to my beloved family members, especially my father, Mr. Inderan Velu, my late mother, Mdm. Diawani Muniandy and my loving husband, Mr. Anilarasu Amaranazan for their endless financial and moral support. My special thanks to my two little sisters Puganeswary and Pavitra, who always there for me whenever I need help. They are my pillar of strength. Last but not least, I wish to dedicate this thesis to my both superhero sons, Arrjun Rudra and Arrihan Rudra, and my precious daughter Arrditri Rudra for waiting patiently for the completion of my PhD journey.

TABLE OF CONTENTS

ACKNOWLEDGEMENT	ii
TABLE OF CONTENTS	iii
LIST OF TABLES	ix
LIST OF FIGURES	xi
LIST OF PLATES	xvi
LIST OF SCHEMES	xvii
LIST OF SYMBOLS	xviii
ABSTRAK	xx
ABSTRACT	xxii
CHAPTER 1 INTRODUCTION	1
1.1 Overview	1
1.2 Problem statement	5
1.3 Research objectives	7
1.4 Outline of thesis	8
CHAPTER 2 LITERATURE REVIEW	10
2.1 Metal oxide gas sensors	10
2.2 One dimensional (1D) metal oxide nanostructured gas sensor	11
2.3 Tin(IV) oxide (SnO ₂)	14
2.3.1 Crystal structure of SnO ₂	14
2.3.2 Physical properties of SnO ₂	15
2.3.3 Gas sensing mechanism of SnO ₂ gas sensor	16
2.3.3(a) The effect of small grain size of SnO ₂ sensor material	21
2.3.3(b) Mechanisms of gas sensing in metal doped SnO ₂ nanostructures	22
2.3.4 Metal additives (dopants) in SnO ₂ gas sensors	24

2.3.4(a)	Ferum doped SnO ₂	25
2.3.4(b)	Cobalt doped SnO ₂	27
2.3.4(c)	Nickel doped SnO ₂	29
2.3.5	Noble metal doped SnO ₂	32
2.3.5(a)	Palladium doped SnO ₂	34
2.3.6	The importance of SnO ₂ as ethanol gas sensor	38
2.3.7	Synthesis methods of SnO ₂ nanostructures	42
2.3.7(a)	Chemical vapour deposition	44
2.3.7(b)	Physical vapour deposition	45
2.3.7(c)	Screen printing technique	46
2.3.7(d)	Sol-gel method	46
2.3.7(e)	Hydrothermal method	48
2.3.7(f)	Hydrothermal method: Instrumentation	49
2.3.7(g)	Synthesis of SnO ₂ using hydrothermal method	50
2.4	Semiconducting metal oxide/conducting polymer nanocomposite as gas sensor	52
2.4.1	Polyaniline (PANI)	53
2.4.2	SnO ₂ /PANI nanocomposite gas sensors	54
2.5	The electrospinning technique	56
2.5.1	Synthesis of PANI nanocomposite fibres by using electrospinning technique	58
2.6	Gas sensor devices	59
	CHAPTER 3 MATERIALS AND EXPERIMENTAL METHODS	62
3.1	Overview	62
3.2	Chemicals and reagents	63
3.3	Laboratory instruments and equipment	63
3.4	Hydrothermal synthesis	65
3.4.1	Preparation of solutions	65

3.4.2	Synthesis of pure tin(IV) oxide (SnO ₂) nanorods	65
3.4.2(a)	Effect of pH	66
3.4.2(b)	Effect of metal precursor concentration	66
3.4.2(c)	Effect of hydrothermal treatment duration	67
3.5	Synthesis of doped tin(IV) oxide nanorods	67
3.6	Synthesis of electrospun SnO ₂ /polyaniline/poly-3-hydroxybutyrate (P3HB) nanocomposite fibres	68
3.6.1	Preparation of solution	68
3.6.2	Synthesis of SnO ₂ /PANI nanocomposite	68
3.6.3	Synthesis of poly-3-hydroxybutyrate (P3HB) biopolymer	69
3.6.4	Preparation of SnO ₂ /PANI/P3HB nanocomposite solution	70
3.6.5	Electrospinning of SnO ₂ /PANI/P3HB nanocomposite fibres	70
3.7	Gas sensing test	72
3.7.1	Gas sensing measurement system	72
3.7.2	The gas sensing properties	73
3.7.3	Fabrication of gas sensor	74
3.7.4	Gas sensing performance measurement	75
3.8	Sample characterisations	76
3.8.1	Fourier transform infrared (FTIR) spectroscopy	76
3.8.2	Ultraviolet-visible diffuse reflectance spectroscopy (UV-vis DRS)	76
3.8.3	Field emission scanning electron microscopy (FESEM) and scanning electron microscopy (SEM) with energy-dispersive X-ray (EDX)	77
3.8.4	High-resolution transmission electron microscopy (HRTEM) and selected area electron diffraction (SAED)	78
3.8.5	X-ray diffraction (XRD)	78
3.8.6	X-ray photoelectron spectroscopy (XPS)	80
3.8.7	Optical microscope	80
3.9	Experimental Approach	81

CHAPTER 4 RESULTS AND DISCUSSION	
 HYDROTHERMAL SYNTHESIS OF PURE TIN(IV)	
 OXIDE (SnO₂) NANORODS AND THE GAS SENSING	
 PROPERTIES	83
4.1 Introduction	83
4.2 Effect of pH on the morphology of pure SnO ₂	83
4.2.1 Field emission scanning electron microscopy (FESEM)	84
4.3 Effect of concentration of precursor	85
4.3.1 Field emission scanning electron microscopy (FESEM)	86
4.3.2 Transmission electron microscopy (TEM)	87
4.4 Effect of duration of heat treatment	88
4.4.1 X-ray Diffraction (XRD)	89
4.4.2 Fourier transform Infrared spectroscopy (FTIR)	91
4.4.3 Field emission scanning electron microscopy (FESEM)	92
4.4.4 Ultraviolet-visible diffuse reflectance spectroscopy (UV-vis DRS)	95
4.4.5 High resolution transmission electron microscopy with selected area electron diffraction (HRTEM/SAED)	96
4.4.6 X-ray photoelectron spectroscopy (XPS)	97
4.5 Possible formation mechanism of pure SnO ₂ <i>via</i> hydrothermal treatment	99
4.6 The possible growth mechanism of pure SnO ₂ nanorods	101
4.7 The gas sensing properties of SnO ₂	102
4.8 The possible mechanism of ethanol gas sensing	104
4.9 Summary	105
CHAPTER 5 RESULTS AND DISCUSSION	
 HYDROTHERMAL SYNTHESIS OF (FE, CO, NI AND PD)	
 DOPED TIN(IV) OXIDE (SnO₂) NANORODS AND THE	
 GAS SENSING PROPERTIES	107
5.1 Introduction	107
5.2 Ferum doped SnO ₂	108
5.2.1 X-ray powder diffraction (XRD)	108

5.2.2	Fourier Transform Infrared (FTIR) spectroscopy	111
5.2.3	Ultraviolet-visible diffuse reflectance spectroscopy (UV-vis DRS)	112
5.2.4	X-ray photoelectron spectroscopy (XPS)	113
5.3	Cobalt doped SnO ₂	116
5.3.1	X-ray powder diffraction (XRD)	116
5.3.2	Fourier Transform Infrared (FTIR) spectroscopy	119
5.3.3	Ultraviolet-visible diffuse reflectance spectroscopy (UV-vis DRS)	120
5.3.4	X-ray photoelectron spectroscopy (XPS)	122
5.4	Ni doped SnO ₂	124
5.4.1	X-ray powder diffraction (XRD)	124
5.4.2	Fourier Transform Infrared (FTIR) spectroscopy	127
5.4.3	Ultraviolet-visible diffuse reflectance spectroscopy (UV-vis DRS)	128
5.4.4	X-ray photoelectron spectroscopy (XPS)	129
5.5	Pd doped SnO ₂	131
5.5.1	X-ray powder diffraction (XRD)	131
5.5.2	Fourier Transform Infrared (FTIR) spectroscopy	133
5.5.3	Ultraviolet-visible diffuse reflectance spectroscopy (UV-vis DRS)	135
5.5.4	X-ray photoelectron spectroscopy (XPS)	136
5.6	The effect of dopants on the surface morphology of (Fe, Co, Ni and Pd) doped SnO ₂ nanostructures	139
5.6.1	Scanning electron microscope (SEM)	139
5.6.2	High resolution transmission electron microscopy with selected area electron diffraction (HRTEM/SAED)	141
5.7	The possible formation of metal doped SnO ₂ nanorods	148
5.8	Ethanol Gas sensing properties of doped SnO ₂	149
5.8.1	Comparison of ethanol gas sensing response of 5Ni:SnO ₂ and 5Pd:SnO ₂ nanorods sensors	152
5.8.2	Gas sensing mechanism for 5Ni:SnO ₂ nanorods sensor	155

5.9	Summary	157
CHAPTER 6 RESULTS AND DISCUSSION		
ELECTROSPUN PD DOPED SnO₂ /POLYANILINE (PANI) /POLY-3-HYDROXYBUTYRATE (P3HB) NANOCOMPOSITE FOR ETHANOL GAS SENSOR		160
6.1	Introduction	160
6.2	Formation of undoped SnO ₂ /PANI/P3HB nanocomposite fibres	160
6.3	Ethanol gas sensing measurement	162
6.4	Scanning electron Microscopy (SEM)	166
6.5	X-ray diffraction (XRD)	167
6.6	Fourier Transform Infrared (FTIR) spectroscopy	169
6.7	X-ray photoelectron spectroscopy (XPS)	171
6.8	Ethanol gas sensing mechanism of Pd:SnO ₂ /PANI/P3HB nanocomposite fibres sensor	175
6.9	Summary	178
CHAPTER 7 CONCLUSIONS AND FUTURE WORK RECOMMENDATION		180
7.1	Conclusions	180
7.2	Recommendation for future studies	182
REFERENCES		183
APPENDICES		
LIST OF PUBLICATIONS		

LIST OF TABLES

		Page
Table 2.1	Resistance variation over time at 290 °C in air (Qin <i>et al.</i> , 2008).	12
Table 2.2	The gas sensing performance of 1D metal oxide nanostructures.	14
Table 2.3	Summary of physical properties of SnO ₂ .	16
Table 2.4	Ni doped SnO ₂ gas sensors synthesis method, particle size and corresponding sensor sensitivity.	32
Table 2.5	Pd doped SnO ₂ gas sensor synthesis method, particle size and corresponding sensor sensitivity.	37
Table 2.6	The physical properties and limit values of VOCs (National Institute for Occupational Safety and Health. <i>et al.</i> , 2012).	40
Table 2.7	The ethanol sensing properties of SnO ₂ nanostructures-based gas sensor.	42
Table 2.8	Various synthesis techniques of SnO ₂ and doped SnO ₂ nanostructures for gas sensing applications.	43
Table 2.9	Electrospinning parameters and their effects on the fibres' morphology (Eftekhari, 2011).	57
Table 3.1	The flow rate of C ₂ H ₂ OH/N ₂ gas and N ₂ gas at desired C ₂ H ₂ OH/N ₂ gas concentrations.	76
Table 4.1	Crystallite size and lattice parameters of SnO ₂ nanostructures prepared at different duration of heat treatment.	91
Table 4.2	Peaks assigned from FTIR spectra.	92
Table 4.3	The binding energy (eV) data obtained from XPS. All spectra were corrected using C1s line at 284.6 eV.	98
Table 4.4	Peaks assignment from the FTIR spectra.	99
Table 5.1	The crystallographic parameters calculated from XRD data of undoped and Fe doped SnO ₂ samples.	110
Table 5.2	Comparison of binding energy data obtained from XPS result for undoped SnO ₂ and 5Fe:SnO ₂ samples. All the data	

	was corrected by referencing the spectra to the standard peak of C 1s at 284.6 eV.	116
Table 5.3	The crystallographic parameters calculated from XRD data of undoped SnO ₂ and Co doped SnO ₂ samples.	118
Table 5.4	The binding energy data obtained from XPS result. All the data was corrected by referencing the spectra to the standard peak of C 1s at 284.6 eV.	124
Table 5.5	The crystallographic parameters calculated from XRD data of undoped SnO ₂ and Co doped SnO ₂ samples.	126
Table 5.6	The binding energy data obtained from XPS result. All the data was corrected by referencing the spectra to the standard peak of C 1s at 284.6 eV.	131
Table 5.7	The crystallographic parameters calculated from XRD data of undoped SnO ₂ and Pd doped SnO ₂ samples.	133
Table 5.8	The binding energy data obtained from XPS result. All the data was corrected by referencing the spectra to the standard peak of C 1s at 284.6 eV.	139
Table 5.9	Data summary of morphology and structural analysis of undoped and doped SnO ₂ samples.	147
Table 5.10	Ethanol gas response data obtained for undoped and doped SnO ₂ nanorods sensor.	152
Table 5.11	Comparison of ethanol gas sensing performance of 5Ni:SnO ₂ and 5Pd:snO ₂ nanorods gas sensor.	154
Table 6.1	Average diameter of fibre at different applied voltage and flow rate.	162
Table 6.2	Ethanol gas sensing measurement of 5Pd:SnO ₂ /PANI/P3HB at different concentration and at operating temperature of 80 °C.	165
Table 6.3	The binding energy data obtained from XPS result. All the data was corrected by referencing the spectra to the standard peak of C 1s at 284.6 eV.	173

LIST OF FIGURES

	Page	
Figure 2.1	The crystal structures of SnO ₂ (red: oxygen atom and blue: tin atom) : (a) rutile tetragonal (<i>P4₂/mnm</i>) and CaCl ₂ -type (<i>Pnmm</i>), (b) α -PbO ₂ -type (<i>Pbcn</i>), (c) pyrite-type (<i>Pa3</i>), (d) ZrO ₂ -type orthorhombic phase I (<i>Pbca</i>), (e) fluorite-type (<i>Fm3m</i>) and (f) cotunnite-type orthorhombic phase II (<i>Pnam</i>) Ref: (Gracia <i>et al.</i> , 2007).	15
Figure 2.2	Schematic diagram of band bending near surface region of SnO ₂ after the chemisorption of oxygen molecules from air. E _c , E _v and E _f respectively denote the energy of conduction band, valence band and the Fermi level. Meanwhile, Λ_{air} indicates the thickness of depletion of electron layer and eV _{surface} signifies the surface potential barrier (adapted from (Yulianto <i>et al.</i> , 2015)).	18
Figure 2.3	Schematic diagram of the reducing gas sensing mechanism on the SnO ₂ surface (Tangirala <i>et al.</i> , 2017).	20
Figure 2.4	The schematic model of the effect of the crystallite size on the sensitivity of SnO ₂ gas sensors: (a) Boundary-controlling model, (b) Neck controlling model and (c) Grain-controlling model (Sun <i>et al.</i> , 2012)	22
Figure 2.5	Schematic diagram of the electronic and catalytic mechanisms in metal doped SnO ₂ . R represents reducing gas (Tangirala <i>et al.</i> , 2017).	24
Figure 2.6	(a) Digital breath analyser and (b) MQ-3 ethanol gas sensor. (Breathalyser Sales and service, 2018)	41
Figure 2.7	Teflon-lined stainless steel chamber (Techinstro Vision Beyond Technology, 2012).	49
Figure 2.8	The design structure of (a) planar layout and (b) cylindrical conductometric gas sensors Ref: (Sun <i>et al.</i> , 2012).	61
Figure 3.1	The synthesis of electrospun SnO ₂ /PANI/P3HB nanocomposite fibres.	72
Figure 3.2	Schematic diagram of gas sensing measurement system.	73
Figure 3.3	Flow chart of the experimental procedure.	82
Figure 4.1	FESEM images of pure SnO ₂ samples synthesised at (a) pH 12 and (b) pH 13, respectively.	85

Figure 4.2	The secondary electron FESEM images of pure SnO ₂ nanostructures prepared at various metal precursor concentrations of SnCl ₄ .5H ₂ O: (a) 0.04 M, (b) 0.08 M (c) 0.12 M (d) 0.16 M and (e) 0.20 M.	87
Figure 4.3	TEM images of SnO ₂ nanostructures samples synthesised at different concentrations of precursor: (a,c) 0.08 M and (b,d) 0.12 M.	88
Figure 4.4	XRD patterns of (a) SnO ₂ -6 hrs, (b) SnO ₂ -12 hrs, (c) SnO ₂ -18 hrs and (d) SnO ₂ -24 hrs. (Ref: ICSD092552).	90
Figure 4.5	FTIR spectra of r (a) SnO ₂ -6 hrs, (b) SnO ₂ -12 hrs, (c) SnO ₂ -18 hrs and (d) SnO ₂ -24 hrs, respectively.	92
Figure 4.6	FESEM images and corresponding EDX patterns of (a) SnO ₂ -6 hrs, (b) SnO ₂ -12 hrs, (c) SnO ₂ -18 hrs and (d) SnO ₂ -24 hrs, respectively.	94
Figure 4.7	The calculated band gap of SnO ₂ nanostructures synthesised at different heating times.	95
Figure 4.8	HRTEM images of samples prepared at 24 hrs under (a) low magnification (38 kx), (b) and (c) high magnification 97 kx and 690 kx, respectively. (d) SAED pattern of region of interest is as shown in the HRTEM image (c).	96
Figure 4.9	High resolution XPS spectra of pure SnO ₂ heat treated at 24 hrs.	98
Figure 4.10	FTIR spectra of pure SnO ₂ sample synthesised with 0.12 M precursor (a) before and (b) after hydrothermal treatment.	99
Figure 4.11	Possible growth mechanism of pure SnO ₂ nanorods.	102
Figure 4.12	The resistance of pure SnO ₂ nanorods at (a) 200 °C, (b) 250 °C, (c) 300 °C, (d) 350 °C, (e) 400 °C and (f) 450 °C.	103
Figure 4.13	The ethanol gas response of pure SnO ₂ nanorods sensor at different operating temperatures.	104
Figure 4.14	The possible ethanol gas sensing mechanism using SnO ₂ nanorods gas sensor.	105
Figure 5.1	Physical appearance of (a) undoped SnO ₂ , (b) Fe doped SnO ₂ , (c) Co doped SnO ₂ , (d) Ni doped SnO ₂ and (e) Pd doped SnO ₂ powder samples.	108
Figure 5.2	XRD diffraction patterns of as-synthesised SnO ₂ samples: (a) undoped SnO ₂ (b) 0.5Fe:SnO ₂ , (c) 1Fe:SnO ₂ , (d) 3Fe:SnO ₂ and (e) 5Fe:SnO ₂	110

Figure 5.3	FTIR spectra of (a) undoped SnO ₂ (b) 0.5Fe:SnO ₂ , (c) 1Fe:SnO ₂ , (d) 3Fe:SnO ₂ and (e)5Fe:SnO ₂ samples.	112
Figure 5.4	$(\alpha h\nu)^2$ as a function of photon energy ($h\nu$) of as-synthesised Fe doped SnO ₂ samples. The band gap energy was obtained by extrapolating the linear region of graph at $(\alpha h\nu)^2=0$.	113
Figure 5.5	High resolution of XPS spectra of (a) Sn 3d, (b) O 1s and (c) Fe 2p for SnO ₂ nanorods	114
Figure 5.6.	XRD patterns of as-synthesised SnO ₂ samples: (a) undoped SnO ₂ (b) 0.5Co:SnO ₂ , (c) 1Co:SnO ₂ , (d) 3Co:SnO ₂ and (e) 5Co:SnO ₂	117
Figure 5.7	FTIR spectra of (a) undoped SnO ₂ (b) 0.5Co:SnO ₂ , (c) 1Co:SnO ₂ , (d) 3Co:SnO ₂ and (e) 5Co:SnO ₂ .	120
Figure 5.8	$(\alpha h\nu)^2$ as a function of photon energy ($h\nu$) of as-synthesised Co doped SnO ₂ samples. The band gap energy was obtained by extrapolating the linear region of graph at $(\alpha h\nu)^2=0$.	121
Figure 5.9	High resolution XPS spectra of (a) Sn 3d, (b) O 1s and (c) Co 2p for 5Co:SnO ₂ nanorods sample.	123
Figure 5.10	XRD patterns of as-synthesised SnO ₂ samples: (a) undoped SnO ₂ (b) 0.5Ni:SnO ₂ , (c) 1Ni:SnO ₂ , (d) 3Ni:SnO ₂ and (e) 5Ni:SnO ₂ .	126
Figure 5.11	FTIR spectra of (a) undoped SnO ₂ (b) 0.5Ni:SnO ₂ , (c) 1Ni:SnO ₂ , (d) 3Ni:SnO ₂ and (e)5Ni:SnO ₂ , respectively.	127
Figure 5.12	$(\alpha h\nu)^2$ as a function of photon energy ($h\nu$) of as-synthesised Ni doped SnO ₂ samples. The band gap energies of all the as-synthesised Ni doped SnO ₂ samples were obtained by extrapolating the linear region of graph at $(\alpha h\nu)^2=0$.	129
Figure 5.13	High resolution XPS spectra of (a) Sn 3d, (b) O 1s and (c) Ni 2p for 5Ni:SnO ₂ sample.	130
Figure 5.14	XRD patterns of as-synthesised SnO ₂ samples: (a) undoped SnO ₂ (b) 0.5Pd:SnO ₂ , (c) 1Pd:SnO ₂ , (d) 3Pd:SnO ₂ and (e) 5Pd:SnO ₂	132
Figure 5.15	FTIR spectra of (a) undoped SnO ₂ (b) 0.5Pd:SnO ₂ , (c) 1Pd:SnO ₂ , (d) 3Pd:SnO ₂ and (e)5Pd:SnO ₂ , respectively.	135
Figure 5.16	$(\alpha h\nu)^2$ as a function of photon energy ($h\nu$) of as-synthesised Pd doped SnO ₂ samples. The band gap energies of all the as-synthesised Pd doped SnO ₂ samples were obtained by extrapolating the linear region of graph at $(\alpha h\nu)^2=0$.	136

Figure 5.17	High resolution XPS spectra of (a) Sn 3d, (b) O 1s and (c) Pd 3d for 5Pd:SnO ₂ sample.	137
Figure 5.18	SEM micrographs of (a) 5 mol% Fe doped SnO ₂ , (b) 5 mol% Co doped SnO ₂ , (c) 5 mol% Ni SnO ₂ and (d) 5 mol% Pd doped SnO ₂ , respectively.	141
Figure 5.19	HRTEM images of 5Fe:SnO ₂ nanorods sample at (a) low magnification (71 Kx), (b) high magnification (285 Kx) (c) lattice fringe (1.05 Mx) and (d) SAED pattern with corresponding planes.	142
Figure 5.20	HRTEM images of 5Co:SnO ₂ nanorods sample at (a) low magnification (43 kx), (b) high magnification (97 kx) (c) lattice fringe (690 kx) and (d) SAED pattern with corresponding planes.	144
Figure 5.21	HRTEM images of 5Ni:SnO ₂ nanorods sample at (a) low magnification (71 kx), (b) high magnification (450 kx) (c) lattice fringe (690 kx) and (d) SAED pattern with corresponding planes.	145
Figure 5.22	HRTEM images of 5Pd:SnO ₂ nanorods sample at (a) low magnification (145 kx) and (b) high magnification (400 kx). (c) lattice fringe (690 kx) and (d) SAED pattern with corresponding planes.	146
Figure 5.23	The resistance curves of as-synthesised undoped and doped SnO ₂ nanorods sensor materials.	150
Figure 5.24	Gas response of 5Ni:SnO ₂ nanorods sensor for different concentration of C ₂ H ₅ OH gas.	153
Figure 5.25	Gas response of 5Pd:SnO ₂ nanorods sensor for different concentrations of C ₂ H ₅ OH gas.	154
Figure 5.26	The ethanol gas sensing mechanism. (a) the adsorption and ionization of oxygen molecules on the surface of 5Ni:SnO ₂ nanorods (b) the reaction between C ₂ H ₅ OH gas and the chemisorbed oxygen ions.	156
Figure 5.27	The ethanol gas sensing mechanism. (a) the adsorption and ionization of oxygen molecules on the surface of 5Pd:SnO ₂ (b) the reaction between C ₂ H ₅ OH gas and the chemisorbed oxygen ions.	157
Figure 6.1	Electrospun undoped SnO ₂ /PANI/P3HB nanocomposite fibres at different applied voltages and flow rates (a) 15 kV; 16.67 µl (b) 18 kV; 3 µl (c) 28 kV; 15 µl.	161
Figure 6.2	The resistance of nanocomposite sensors (a)Undoped SnO ₂ /PANI/P3HB, (b) 5Ni:SnO ₂ /PANI/P3HB and (c)	

	5Pd:SnO ₂ /PANI/P3HB at the operating temperature of 80 °C.	163
Figure 6.3	Real time-response curve of 5Pd:SnO ₂ /PANI/P3HB sensor for different concentration of C ₂ H ₅ OH gas.	165
Figure 6.4	SEM micrograph of electrospun 5Pd:SnO ₂ /PANI/P3HB nanocomposite fibres with (a) 5000 x magnification (inset: fibres diameters distribution) (b) 100000 x magnification (inset: 5Pd:SnO ₂ agglomerates).	167
Figure 6.5	XRD patterns of 5Pd:SnO ₂ , PANI and 5Pd:SnO ₂ /PANI/P3HB nanocomposite fibres.	168
Figure 6.6	FTIR spectra of P3HB, PANI and 5Pd:SnO ₂ /PANI/P3HB nanocomposite fibres.	170
Figure 6.7	High resolution XPS spectra of (a) PANI -N 1s and (b) 5PdSnO ₂ /PANI/P3HB - N 1s. (Al K α X-ray source, 1486.6 eV of photons).	172
Figure 6.8	High resolution XPS spectra of Sn 3d for (a) 5Pd:SnO ₂ nanorods and (b) 5PdSnO ₂ /PANI/P3HB nanocomposite fibres, respectively. (Al K α X-ray source, 1486.6 eV of photons)	174
Figure 6.9	Schematic illustration of the ethanol gas sensing on 5Pd:SnO ₂ /PANI/P3HB nanocomposite sensor. The reaction between the ethanol gas and PANI shown in the inset.(Adapted from Ref. (Gawri <i>et al.</i> , 2018; Quan <i>et al.</i> , 2017)).	177

LIST OF PLATES

	Page
Plate 3.1	
Electrospinning of nanocomposite (a) aluminium foil (b) Au-interdigitated electrode placed on the collecting plate in electrospinning instrument.	71

LIST OF SCHEMES

	Page
Scheme 2.1 Molecular structure of PANI	54
Scheme 2.2 Chemical oxidation polymerisation of aniline to form polyemeraldine salt.	54
Scheme 2.3 Schematic diagram of electrospinning apparatus set up: (a) vertical setup and (b) horizontal setup (Nandana Bhardwaj, 2010).	57
Scheme 6.1 The polymer structure of conductive polymer PANI.	168

LIST OF SYMBOLS

μL	Microliter
\AA	Angstrom
APS	Ammonium persulphate
cm	Centimeter
DAQ	Data acquisition
DMF	N,N- dimethylformamide
e	Electron
eV	Electronvolt
FTIR	Fourier Transform Infrared spectroscopy
g	Gram
hrs	Hours
HRTEM	High resolution transmission electron microscopy
K	Kelvin
kV	Kilovolt
M	Molar
mA	Miliampere
MFC	Mass flow controller
min	Minute
mL	Mililiter
Mol%	Mole percentage
nm	Nanometer
$^{\circ}\text{C}$	Degree Celsius
P3HB	Poly-3-hydroxybutyrate

Pa	Pascal
PANI	polyaniline
R_0	Sensor resistance in background gas
R^2	Correlation coefficient
R_g	Sensor resistance in target gas
s	Second
SAED	Selected area electron diffraction
sccm	standard cubic centimeter per minute
SEM	Scanning electron microscopy
T_{rec}	Recovery time
T_{res}	Response time
UV-vis DRS	Ultraviolet-visible diffuse reflectance spectroscopy
v/v	Volume per volume
W	Watt
Wt%	Weight percentage
XPS	X-ray photoelectron spectroscopy
XRD	X-ray diffraction
PVP	Polyvinylpyrrolidone
PEG	Polyethylene glycol
SDS	Sodium dodecyl sulphate
MW	Molecular weight

**SINTESIS DAN PENCIRIAN NANOKOMPOSIT STANUM(IV) OKSIDA
TERDOP/POLIANILINA/POLIHIDROKSIBUTIRAT ELEKTROPINTAL
SEBAGAI PENDERIA GAS ETANOL**

ABSTRAK

Nanokomposit semikonduktor oksida logam/polimer konduktif ialah satu kelas baru bahan yang menggabungkan kelebihan oksida logam dan polimer. Penderia gas yang berasaskan oksida logam sering memerlukan suhu operasi yang tinggi dan menyebabkan penggunaan kuasa yang tinggi dan tempoh hayat yang singkat. Sebaliknya, polimer konduktif sesuai untuk penggunaan suhu operasi yang rendah, tetapi ia mempunyai tempoh tindak balas yang panjang. Bagi mengatasi kekurangan ini, satu penderia gas baru berasaskan nanokomposit elektropintal telah berjaya dibangunkan dengan menggabungkan nanorod stanum(IV) oksida (SnO_2) dengan polianilina (PANI) dan polihidroksibutirat (P3HB). Bahan tersintesis ini telah diuji dengan gas etanol ($\text{C}_2\text{H}_5\text{OH}$) dengan gas nitrogen (N_2) sebagai gas pembawa. Suatu kaedah mudah hidrotermal telah digunakan untuk mensintesis SnO_2 dan SnO_2 terdop nanorod tanpa acuan organik atau pengaktif permukaan. Kesan daripada pelbagai parameter iaitu pH, kepekatan prekursor dan tempoh pemanasan telah disiasat. Bagi nanorod SnO_2 terdop, kesan daripada pelbagai jenis dopan logam (Fe, Co, Ni, dan Pd) dan kepekatan setiap dopan juga telah dikaji. Keadaan optimum untuk mensintesis SnO_2 adalah 180 °C, pH 13 dengan kepekatan prekursor 0.12 M dan tempoh pemanasan selama 24 jam. Nanorod SnO_2 yang telah disintesis telah diuji dengan 1000 ppm gas $\text{C}_2\text{H}_5\text{OH}$ pada suhu operasi yang berbeza (200 – 450 °C) dan ia memaparkan tindak balas yang paling tinggi ($R_a/R_g, 1.1 \times 10^3$) pada suhu 450 °C dengan tempoh tindak balas, T_{res} , 60 s. Bagi SnO_2 terdop, perubahan pada parameter hablur menonjol

apabila kepekatan dopan meningkat, dengan struktur hablur tetragon rutil dikekalkan. Ujian pengesanan gas C₂H₅OH pada suhu operasi 450 °C menunjukkan penderia SnO₂ didop dengan 5 mol% Ni (5Ni:SnO₂) dan SnO₂ didop dengan 5 mol% Pd (5Pd:SnO₂) memaparkan tindak balas yang agak tinggi terhadap gas C₂H₅OH (R_0/R_g , 1.4×10^4 and $R_0/R_g, 1.7 \times 10^4$) dengan tempoh tindak balas T_{res} (50 s and 40 s) dan tempoh kembali ke rintangan elektrik asal adalah pantas T_{rec} , (22 min and 12 min) berbanding dengan penderia gas nanorod SnO₂ tanpa didop. Apabila pengesanan dijalankan pada gentian nanokomposit 5Pd:SnO₂/PANI/P3HB, penderia gas mempamerkan ciri pengesanan gas C₂H₅OH yang sangat baik pada suhu 80 °C dengan bacaan R_0/R_g , 1.6×10^3 , T_{res} , 90 s dan T_{rec} , 10 min. Ciri penderia gentian nanokomposit 5Pd:SnO₂/PANI/P3HB ini disebabkan oleh hetero-simpang p-n, bentuk geometri gentian, satu dimensi (1D) nanorod dan kehadiran atom-atom Pd sebagai mangkin yang aktif. Penderia gentian nanokomposit yang baharu ini bakal menjadi satu kejayaan dalam aplikasi penderia gas etanol yang terbiodegradasi dan berfungsi pada suhu rendah.

**SYNTHESIS AND CHARACTERISATION OF ELECTROSPUN DOPED
TIN(V/POLYANILINE/POLYHYDROXYBUTYRATE NANOCOMPOSITE
FOR ETHANOL GAS SENSOR**

ABSTRACT

Semiconducting metal oxide/conducting polymer nanocomposite is a new class of material that combined the advantages of both metal oxide and polymer. Metal oxide based gas sensors tend to require high operating temperature, leading to high power consumption and short life time. In contrast, conductive polymers fit for low operating temperature usage, but they have slower response time. In order to overcome the limitations, a new electrospun nanocomposite based gas sensors were successfully developed by incorporating as-synthesised SnO₂ nanorods into polyaniline (PANI) and polyhydroxybutyrate (P3HB). The as-synthesised materials were tested on ethanol (C₂H₅OH) gas using nitrogen (N₂) as carrier gas. A facile hydrothermal method without using any organic template or surfactant was employed to synthesise undoped and doped SnO₂ nanorods. The effects of various parameters namely pH, precursor concentration and duration of heat treatment were investigated. For the doped SnO₂ nanorods, the effects of different types of metal dopant (Fe, Co, Ni and Pd) and the concentrations of each dopant (0.5, 1.0, 3.0 and 5.0 mol%) were also studied. The optimum condition for the synthesis of SnO₂ nanorods powder was 180 °C, pH 13, with a precursor concentration of 0.12 M and the duration of heat treatment of 24 hrs. The as-synthesised SnO₂ nanorods tested with 1000 ppm C₂H₅OH gas at different operating temperatures (200 – 450 °C) and exhibited the highest response (R_a/R_g , 1.1×10^3) at 450 °C with response time, T_{res} of 60 s. For doped SnO₂, the changes in crystallographic parameters were prominent as the concentration of dopant increased,

while maintaining the rutile tetragonal crystal structure. The C₂H₅OH gas sensing test showed that 5 mol% Ni doped SnO₂ (5Ni:SnO₂) and 5 mol% Pd doped SnO₂ (5Pd:SnO₂) sensors have demonstrated relatively high C₂H₅OH gas response (R_0/R_g , 1.4×10^4 and R_0/R_g , 1.7×10^4) with fast response time, T_{res} , (50 s and 40 s) and recovery time, T_{rec} , (22 min and 12 min) at operating temperature of 450 °C as compared to undoped SnO₂ nanorods sensor. When it is carried out on the 5Pd:SnO₂/PANI/P3HB, the nanocomposite sensor exhibited excellent gas sensing properties at 80 °C with R_0/R_g , 1.6×10^3 , T_{res} , 90 s and T_{rec} , 10 min, respectively. The good sensing properties of 5Pd:SnO₂/PANI/P3HB nanocomposite fibres sensor were mainly attributed to p-n heterojunction, the fibres geometry, one dimensional (1D) nanorods and the presence of catalytic active Pd atoms. This new nanocomposite sensor will be a breakthrough in biodegradable low temperature ethanol sensor applications.

CHAPTER 1

INTRODUCTION

1.1 Overview

In the past couples of decades, the innovation of nanomaterials has become a leading edge in the field of nanoscience and nanotechnology. The nanotechnology defined as the development of functional materials, devices and systems with a dimension in the range of 1-100 nm (Korotcenkov, 2013). With a reduction in size, nanostructured materials exhibit unique properties such as electrical, mechanical and chemical properties which are significantly different from those of their bulk counterparts. To date, a wide variety of nanoscale materials has been synthesised. Among nanostructured semiconductors, metal oxides have received broad attention due to their distinguished properties in optics, gas sensors, magnetics and in catalysis (Batzill and Diebold, 2005).

The application of metal oxides as gas sensors has attracted many researchers attention ever since Seiyama and the co-workers (1962) discovered that the adsorption and desorption of gases on the surface of zinc oxide (ZnO) film caused a rapid changes in electrical conductivity (Seiyama *et al.*, 1962). Since then, various types of metal oxides have been extensively investigated for gas sensing applications. In the early years, gas sensors have been fabricated in the form of thin films, where the metal oxide nanoparticles were coated on electrodes followed by sintering at high temperature (Korotcenkov, 2007). Recently, the one-dimensional (1-D) metal oxide nanostructures are found to be very promising for gas sensing applications due to their very high surface to volume ratio is very high and which can subsequently improve their sensor sensitivity (Pal *et al.*, 2012). Various forms of 1-D metal oxide nanostructures have been synthesised such as nanowires (Qin *et al.*, 2008), nanotubes (Wang *et al.*, 2011),

nanospheres (Tang and Wang, 2016), nanorods (Birkel *et al.*, 2010) and nanobelts (Fields *et al.*, 2006).

Among them, 1-D nanostructured, SnO₂ have received a great deal of interest in gas sensing applications owing to remarkable characteristics such as wide band gap (3.6 eV at 300 K) and high mobility of conduction electrons (100-200 cm² Ve⁻¹ S⁻¹) (Batzill and Diebold, 2005). It is well established that the properties of SnO₂ nanostructures mainly depend on the synthesis route. A number of methods such as thermal evaporation (Luo *et al.*, 2004), hydrothermal (Nasresfahani *et al.*, 2017), chemical vapour deposition (CVD) (Kwoka *et al.*, 2005), sol-gel (Marikutsa *et al.*, 2010) and co-precipitation (Zhang *et al.*, 2005) have been employed to synthesise 1-D SnO₂ nanostructures. Among them, hydrothermal route was considered as a promising method widely used to synthesise homogeneous SnO₂ nanostructures with controlled shape and size. Hydrothermal method is one in which the formation and growth of nanocrystal occurred under high temperature and pressure *via* chemical reaction and the solubility of substances (Shi *et al.*, 2013). Studies showed that tuning the experimental parameters, for instance type of solvent, pH condition, concentration of the precursor, heating temperature and duration of hydrothermal reaction affect the final morphology of product (Shi *et al.*, 2013). Although 1-D SnO₂ nanostructures shows some encouraging results in gas sensor application, improving the poor gas sensing response and recovery time, and high operating temperature require more efforts and still remain as a challenge. Therefore, significant effort has been focused on the improvement of SnO₂-based gas sensors.

One of the most common techniques for enhancing the gas sensing performance is by introducing transition metals or noble metals as a dopant. Noble metals such as Pd and Pt are often used to dop SnO₂ because of their excellent

oxidation catalytic properties which in turn enhance the reaction on the sensor surface during the gas sensing process (Korotcenkov, 2007). Meanwhile, 3d transition metals (e.g Ni, Cu, Co, Fe, etc), doped -SnO₂ have been observed to improve their sensor response, response time and recovery time by reducing the size of SnO₂ particles (Zhao *et al.*, 2015). Nevertheless, those doping sensors still require relatively high operating temperature (above 300 °C).

On the other hand, organic materials especially conductive polymer sensors work very well at room temperature and they are easy to fabricate due to their flexibility (Bai and Shi, 2007). Polyaniline (PANI) is one of the most extensively studied conductive polymers because of its ease preparation, high conductivity, low operating temperature and good environmental stability (Quan *et al.*, 2017). However, PANI alone exhibits a rather low sensitivity to target gas. Recently, Kondawar and co-workers have established SnO₂/PANI nanocomposite for ammonia sensing application (Kondawar *et al.*, 2012). Interestingly, this material is found to demonstrate special properties which is generated from both metal oxide and conductive polymer.

Typically, the synthesis of nanocomposite was carried out by mixing the metal oxide nanopowders with PANI polymer which was later fabricated into thin film (Geng, 2009). In another study by Geng and co-researchers (2007), the hybrid SnO₂/PANI was prepared *via* hydrothermal treatment where PANI was polymerised *in-situ* (Geng *et al.*, 2007). However, these methods could decrease the surface area of sensor materials.

In order to increase the surface area (> 100 cm² g⁻¹) of the sensor materials, electrospinning technique is often an efficient and relatively simple method to produce nanocomposite fibres (Ding *et al.*, 2009). Subsequently, higher surface area of sensor

material leads to higher sensitivity. However, the low molecular weight of PANI is generally insufficient for it to be electrospun directly into the fibres (Zhang and Rutledge, 2012). Thus, to circumvent this problem, the material usually blends together with higher molecular weight polymer such as polyvinylpyrrolidone (PVP) (Song *et al.*, 2009) and poly-3-hydroxybutyrate (P3HB) (Araujo *et al.*, 2011).

Hence in this study, poly-3-hydroxybutyrate (P3HB) is selected. P3HB is a high molecular weight biopolymer that belongs to polyhydroxyalkanoates (PHAs) polymer class which is produced from microbial. A number of studies has been reported on the synthesis of PANI/P3HB conductive polymer which eventually combines both characteristics of biodegradability and electrical semiconductivity with good mechanical properties (Fryczkowski and Kowalczyk, 2009; Araujo *et al.*, 2011; Macagnano *et al.*, 2016).

To date, gas sensor plays a key role in various areas, especially in public and environmental safety, medical therapeutics, pollutants motoring and transportation industries. Ethanol (C_2H_5OH) gas sensors were extensively used in many applications to monitor chemical reactions, biomedical productions as well as breath analyser. Generally, the operating temperature of gas sensor depends on the area of applications. For instance, the operating temperature of the C_2H_5OH sensor in breath analyser is relatively lower than that of the sensor employed in industrial application works.

Herein, this research is divided into two parts: The main part of this research focuses on the synthesis of SnO_2 nanorods using the hydrothermal method and explores the effects of synthesis parameters, namely pH condition, concentration of the precursor and the duration of heat-treatment. The effects of *3d* transition metals doping on the structural and morphological properties of SnO_2 nanorods are then

investigated. The results obtained are compared with those of noble metal (Pd) doped SnO₂ nanorods. The as-synthesised pure and doped SnO₂ nanorods are tested on C₂H₅OH gas sensing in order to relate the properties of sensor material with the C₂H₅OH sensor response. This study will provide a better understanding of the roles of dopants in sensor materials.

Meanwhile, in the second part of the research, inorganic-organic hybrid nanocomposite fibres are synthesised *via* electrospinning technique using as-synthesised SnO₂ nanorods powder, conductive polymer PANI and a biopolymer P3HB. The effect of applied voltage and the flow rate to the polymer solution during the formation of fibres is carefully investigated. Then, this novel nanocomposite sensor is tested on C₂H₅OH gas. The nanostructured sensor materials synthesised in this research have a potential application as C₂H₅OH gas sensor.

1.2 Problem statement

Despite the advantages of SnO₂, its real application in the gas sensor field is still limited and in need of improvement. One of the common routes to improve the sensor properties is to reduce the particle size of SnO₂ to nanoscale. Previous studies have shown that 1-D SnO₂ nanostructures are an excellent candidate for gas sensing applications due to high surface-to-volume ratio (Korotcenkov, 2013). A number of methods were developed to synthesise homogenous SnO₂ nanostructured with controlled shape and size. However, these methods usually involve high temperature, complicated procedures and expensive instrumentation, which consequently increase the cost of sensor materials. Recently, hydrothermal method has been widely used in synthesising 1-D nanostructure metal oxides. However, the usage of surfactants and organic templates such as sodium dodecyl sulphate (SDS) (Tan *et al.*, 2011) and

polyethylene glycol (PEG) (He *et al.*, 2013) can cause environmental problems, especially to aquatic system. Meanwhile, Matin and co-workers (2010) successfully synthesised SnO₂ nanostructures *via* hydrothermal route using neither alkaline solution nor organic templates at 160 °C; however, the samples have to undergo post calcination at high temperature of 350 °C. Thus, in this current research, 1-D SnO₂ nanorods were synthesised using a simple hydrothermal route without using an organic template, surfactant and post calcination (Matin *et al.*, 2010).

Besides 1-D nanostructures, doping with transition metals and noble metals also improve the sensor characteristics of SnO₂ nanostructures. It is well known that adding noble metal dopants such as Pd and Pt lead to tremendous improvement in SnO₂ gas sensing properties (Kappler *et al.*, 1998). Nevertheless, their obvious cost restricts their potential in practical applications. Thus, it was essential to explore less expensive alternatives such as common 3d transition metals (e.g. Fe, Co, Ni, Cu, etc) to reduce the operation cost as well as to enhance the sensing performance. However, transition metals are rarely used than noble metals, even though they could improve the sensing properties of SnO₂. Furthermore, it can be difficult to study the effect of different transition metals doping on the gas sensing properties between numerous studies since the synthesis routes and reaction conditions are different which precludes predicting the final optimised functionality of SnO₂ sensor material. To the best of our knowledge, there is not many comparative studies of sensing properties of transition metals doped SnO₂ has been reported.

On the other hand, although SnO₂ nanostructures are widely used in industrial applications, their crystalline structures are not suitable for fabricating on flexible substrates. In addition, the high operating temperature is the main drawback in pure and doped SnO₂ based gas sensors. PANI is one of the most used organic sensor

material, but its low sensitivity and poor solubility in organic solvent limits its applications (Kondawar *et al.*, 2012). Therefore, a novel electrospun sensor material, SnO₂/PANI/P3HB nanocomposite fibres is being proposed in this study, which can complement the properties of SnO₂ and PANI.

Presently, C₂H₅OH gas detecting and monitoring technologies have attracted increased attention due to their high demand in biomedical, chemical, food industries as well as traffic safety. Therefore, current research was focused on the development of low cost and high-performance C₂H₅OH gas sensor.

1.3 Research objectives

To address the aforementioned shortcoming, the main aim of this research is to develop an efficient and environmentally friendly gas sensor nanomaterial. In order to achieve this goal, it is essential to understand the fundamental relationship between sensor response and physico properties of SnO₂ nanorods. Therefore, the specific objectives of this research are as follows:

- i. To synthesise and study the structural and morphological characteristics of pure SnO₂ nanorods under different reaction parameters *via* hydrothermal method.
- ii. To study the effect of different dopants (Fe, Co, Ni and Pd) on the morphology and structure of SnO₂ nanorods.
- iii. To conduct comprehensive studies on the ethanol gas sensing performance of as-synthesised pure and doped-SnO₂ samples.
- iv. To fabricate SnO₂/PANI/P3HB nanocomposite fibres using electrospinning method and characterise these nanofibres using spectroscopy and microscopy techniques.

- v. To investigate the ethanol gas sensing properties of these SnO₂/PANI/P3HB nanocomposite fibres and propose the gas sensing mechanisms of these samples.

1.4 Outline of thesis

This thesis consists of seven chapters and is presented as follows:

Chapter 1 gives an overview of the study. It mainly focuses on the problem statements, research objectives and outline of the content.

Chapter 2 is a detailed literature review related to SnO₂ nanostructures in gas sensor application, the doped SnO₂ sensor properties, gas sensing mechanism, the principle of hydrothermal method and electrospun polymer nanocomposite fibres. The justification for author's research rationale is explained.

Chapter 3 is concerned with the methodology used for this study. Firstly, the steps involve in the fabrication of the pure SnO₂ and doped nanorods sensor materials are laid out. In addition, the technique employed for the novel SnO₂/PANI/P3HB nanocomposite as well as C₂H₅OH gas sensing measurement are discussed. The basic principles of the instrumental characterisation methods by Fourier transform infrared spectroscopy (FTIR), X-ray powder diffraction (XRD), X-ray photoelectron spectroscopy (XPS), field emission scanning electron microscopy (FESEM), scanning electron microscopy (SEM) coupled with energy-dispersive X-ray spectroscopy (SEM/EDX), high resolution transmission electron microscopy with selected area electron diffraction (HRTEM/SAED), ultraviolet-visible spectroscopy (UV-vis) was also explained in this chapter.

Chapter 4 discusses the characterisation results obtained for pure SnO₂ nanorods sample synthesised *via* hydrothermal method at different conditions (pH condition, concentration of the precursor and duration of heat treatment). The optimum condition for the SnO₂ nanorods synthesis was stated and a possible growth mechanism is described in detail.

Chapter 5 presents the results and discussion of (Fe³⁺, Co²⁺, Ni²⁺ and Pd²⁺) doped SnO₂ nanorods samples prepared *via* hydrothermal method using various dosages of dopants. The experimental results obtained from C₂H₅OH gas sensing measurement are reported. The role of dopants on the sensor performance is discussed and the gas sensing mechanism is suggested.

Chapter 6 discusses the optimum condition for fabricating electrospun SnO₂/PANI/P3HB. The C₂H₅OH gas sensing performance of novel nanocomposite fibre SnO₂/PANI/P3HB is investigated. The characteristics of the best performed nanocomposite fibres are discussed.

Chapter 7 presents the conclusions and possible future works.

CHAPTER 2

LITERATURE REVIEW

2.1 Metal oxide gas sensors

Metal oxides gas sensors are receiving much attention in both industrial and environmental fields. They are widely used in industrial productions, automotive industries, medical applications, indoor air quality supervision and environmental monitoring applications (Miller *et al.*, 2014). The selection of metal oxide for gas sensor applications depends on their electronic structure. Generally, metal oxides can be divided into two groups, namely transition metal oxides (e.g Fe₂O₃, NiO, Cr₂O₃, etc.) and non-transition metal oxides which include pre-transition metal oxides (e.g Al₂O₃, etc) and post transition metal oxides (e.g. ZnO, SnO₂, etc.) (Henrich and Cox, 1994). Pre-transition metal oxides are known as wide band gap insulators and are expected to be inert. This is because with large band gap (~6.7 eV) neither electrons nor holes can easily be formed. Thus, this group of metal oxides is seldom used as gas sensors due to poor electrical conductivity (Yurish, 2012). On the other hand, transition metal oxides behave differently because the energy difference between each oxidation state of cation (d^n , d^{n+1} and d^{n-1}) is considerably small, where they can exist in several different kinds of oxides. However, the structural instability and non-optimality of other parameters which are important in gas sensors limit their application (Wang *et al.*, 2010). Unlike transition metals, only transition metal oxides with d^0 and d^{10} electronic configurations could find the real applications in gas sensor field. The d^0 electron configuration found in binary transition-metal oxides such as TiO₂, V₂O₅ and WO₃. Whereas, d^{10} configuration is found in post-transition metal oxides, such as ZnO, In₂O₃ and SnO₂, which are active in redox reaction because the electron configuration may be altered (Korotchenkov, 2013).

In past few decades, many papers about metal oxide gas sensors have been published. They are used for detecting various oxidising and reducing gases. According to Choi and Jang (2010) survey, tin(IV) oxide (SnO_2) remains the most frequently employed metal oxide in gas sensor applications, which is about 42% of publication in the last three decades, along with ZnO (16%), TiO_2 (13%), WO_3 (9%) and In_2O_3 (7%), respectively. These metal oxides are followed by Fe_2O_3 , CuO, NiO, Ga_2O_3 and V_2O_5 (Choi and Jang, 2010). The predominance of SnO_2 is due to the fact that this material is sensitive to practically all flammable or toxic gases.

2.2 One dimensional (1D) metal oxide nanostructured gas sensor

One dimensional (1D) metal oxide nanostructures including nanowires, nanorods, nanotubes, nanobelts and nanoribbons have been regarded as the most promising materials for gas sensor applications due to their high surface-to-volume ratio and high crystallinity (Pearson and Ren, 2013). In addition, single phase 1D nanostructures such as nanobelts and nanowires, a detail analysis of the gas surface interaction can be carried out because there are no necks and boundaries. In contrast, the sensor system consists of randomly aggregated metal oxide nanoparticles with non-uniform particle size distributions, making it difficult to study the gas sensing properties accurately (Korotchenkov, 2013).

Several studies of 1D metal oxides nanostructured gas sensor can be found in literature review. Qin and co-researchers (2008) stated that powdered polycrystalline SnO_2 sensors are less stable because of the growth and agglomeration of grains. Whereas this origin for instability should not be relevant to 1D SnO_2 morphology with single crystalline. Table 2.1 presents the stability result for SnO_2 nanowires prepared by Qin and co-researchers (2008). The result revealed that the SnO_2 nanowires exhibit

a stable resistance reading over an eight–days period in ambient air at 290 °C. It was deduced that the annealing treatment process and the excellent thermal stability of 1D SnO₂ nanowires could attribute to good stability of the gas sensor (Qin *et al.*, 2008).

Table 2.1: Resistance variation over time at 290 °C in air (Qin *et al.*, 2008).

Day	1	2	4	7	8
Resistance (MΩ)	13.3	13.6	13.5	13.8	13.9

In another study Chen and co-researchers (2006), synthesised SnO₂ nanoparticles and nanorods with similar size (<6 nm) using hydrothermal route and conducted gas sensing test on ethanol gas. They observed that SnO₂ nanorods recorded high response ($R_a/R_g = 83.3$) towards ethanol gas at 300 °C, but surprisingly no measurement signal was detected for SnO₂ nanoparticles. It was then suggested in SnO₂ the decreased in carrier mobility is due to the large amount of nanoparticle which interfaces caused an increase in resistance. Meanwhile, the high sensitivity of nanorods was related to the diameter of particle which is almost close to 2L (L, width of depletion layer) of SnO₂ (3 nm). Hence, more oxygen in the atmosphere adsorbed on the sensor surface and lead to almost complete electron depletion in the nanorods. This phenomenon caused a drastic improvement towards ethanol gas (Chen *et al.*, 2006).

On the same note, Xi and Ye (2010) synthesised ultrathin nanorods with average diameter of ~2 nm which is smaller than its exciton Bohr radius. They also evaluated the ethanol gas sensing performance with nanowires, nanobelts and microrods by maintaining the experiment parameters. It was found that the ultrathin SnO₂ nanorods exhibited the highest ethanol sensing response (R_a/R_g 62 to 200 ppm), among the other SnO₂ nanostructures (nanowires, R_a/R_g 45 to 200 ppm and nanobelts,

R_a/R_g 23 to 200 ppm). However, the authors did not mention the size of other nanostructures (Xi and Ye, 2010).

Furthermore, by controlling the faceting planes of metal oxide 1D nanostructures, one can improve the sensitivity, selectivity and decrease humidity effects in gas sensors (Korotchenkov, 2013). Maiti and co-workers (2003) reported that SnO₂ nanoribbons with exposed (10 $\bar{1}$) and (010) surfaces demonstrated highly effective NO₂ sensing properties. The sensing mechanism was examined using first principles density functional theory (DFT) calculation (Maiti *et al.*, 2003). In the preparation of polycrystalline metal oxides, it is difficult to control the grain facet. However, it is achievable for 1D nanostructures metal oxide gas sensors. It was reported that the planes and faceting in 1D metal oxides nanostructures are subjected to the synthesis parameters (Wang *et al.*, 2013).

Up to now, various 1D metal oxide nanostructures have been fabricated into gas sensors. Table 2.2 presents the most used 1D metal oxide nanostructures in gas sensor researches. In summary, 1D metal oxide sensing materials show several advantages, such as facile fabrication, high surface area ($\sim 100 \text{ cm}^2 \text{ g}^{-1}$) (Matin *et al.*, 2010), high sensitivity and long-term stability, which make them prospective material for high quality gas sensor.

Table 2.2: The gas sensing performance of 1D metal oxide nanostructures.

Material	Target gases	Sensitivity (concentration, ppm)	Average diameter (nm)	Operating temperature (°C)	Ref.
SnO ₂ nanobelts	ethanol	6.2 (100)	50–100	210	(Huang <i>et al.</i> , 2017)
SnO ₂ nanobelts	ethanol	41.6 (250)	~200	400	(Comini <i>et al.</i> , 2002)
SnO ₂ nanobelts	NO ₂	15.5 (0.5)	~200	400	(Comini <i>et al.</i> , 2002)
SnO ₂ nanorods	ethanol	213 (100)	5–20	200	(Shi <i>et al.</i> , 2009)
SnO ₂ nanowires	H ₂	253.0 (1000)	3–200	100	(Shen <i>et al.</i> , 2009)
SnO ₂ nanotubes	H ₂ S	22 (10)	12 – 14	300	(Cho <i>et al.</i> , 2017)
ZnO nanorods	H ₂	53.7 (3000)	~66	150	(Sett and Basak, 2017)
ZnO nanowires	NO ₂	90.9 (0.5)	N/A	225	(Ahn <i>et al.</i> , 2008)
ZnO nanobelts	NO	54 (50)	100–200	200	(Kaur <i>et al.</i> , 2017)
WO ₃ nanorods	NO ₂	3.39 (10)	200	300	(Park <i>et al.</i> , 2012)
WO ₃ nanorods	CO	2.38 (30)	200	300	(Park <i>et al.</i> , 2012)
In ₂ O ₃ nanowires	ethanol	80 (50)	100	200	(López-Aymerich <i>et al.</i> , 2017)

2.3 Tin(IV) oxide (SnO₂)

2.3.1 Crystal structure of SnO₂

In general, SnO₂ has several polymorphs which are rutile tetragonal, CaCl₂-type, α -PbO₂-type, pyrite-type, ZrO₂-type orthorhombic phase I, fluorite-type and cotunnite-type orthorhombic phase II (Das and Jayaraman, 2014). Gracia and team (2007) reported that as the pressure increased SnO₂ underwent a transition from rutile-type \rightarrow CaCl₂-type \rightarrow α -PbO₂-type \rightarrow pyrite-type \rightarrow ZrO₂-type orthorhombic phase I

→ fluorite-type and cotunnite-type orthorhombic phase II (Gracia *et al.*, 2007). Among all these structures rutile tetragonal found to be the most stable phase (Appendix 1). Figure 2.1 shows the simulated crystal structures of SnO₂. Naturally, rutile SnO₂ occurs in mineral form, called as Cassiterite. Rutile SnO₂ has lattice parameters of $a = b = 4.737 \text{ \AA}$ and $c = 3.186 \text{ \AA}$ (in the tetragonal structure, $a = b$) and a unit cell with a space-group symmetry of $P4_2/mnm$. The position of atoms in crystal structure is determined by the ratio of lattice parameters c/a as well as internal parameter u . The position of cations (Sn) are at $(0\ 0\ 0)$ and $(\frac{1}{2}\ \frac{1}{2}\ \frac{1}{2})$ and are surrounded by a distorted octahedron of anions (O) (Wu *et al.*, 2010).

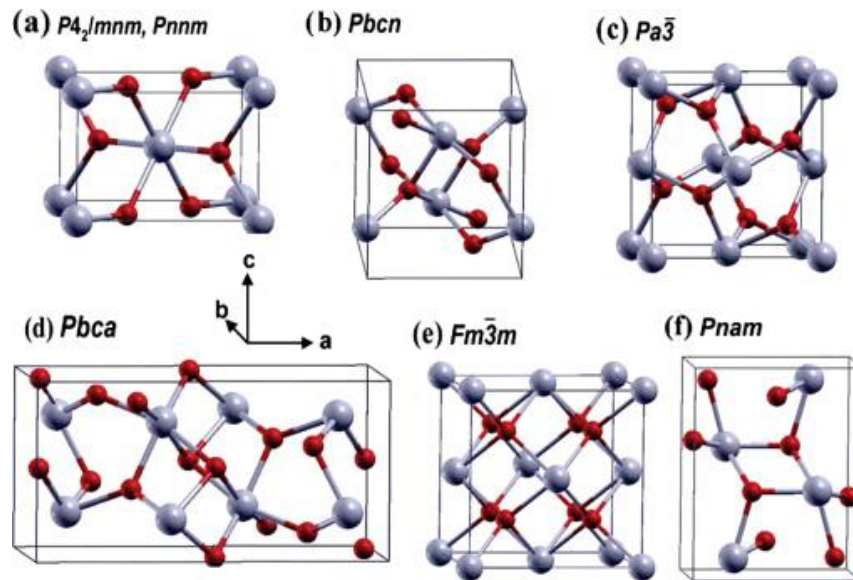


Figure 2.1: The crystal structures of SnO₂ (red: oxygen atom and blue: tin atom) : (a) rutile tetragonal ($P4_2/mnm$) and CaCl₂-type ($Pnnm$), (b) α -PbO₂-type ($Pbcn$), (c) pyrite-type ($Pa\bar{3}$), (d) ZrO₂-type orthorhombic phase I ($Pbca$), (e) fluorite-type ($Fm\bar{3}m$) and (f) cotunnite-type orthorhombic phase II ($Pnam$) Ref: (Gracia *et al.*, 2007).

2.3.2 Physical properties of SnO₂

Tin(IV) oxide (SnO₂) belongs to n-type semiconductor with wide band gap. It has been studied with great attention due to its high transparency in visible range of

electromagnetic spectrum, high reflectivity in infrared region and enhanced gas sensing properties that combine with low electrical resistance (Ahmad *et al.*, 2016).

Table 2.3 presents a summary of physical properties of SnO₂.

Table 2.3: Summary of physical properties of SnO₂.

Properties	Descriptions
Mineral name	Cassiterite
Crystal structure	Tetragonal, rutile
Space group	P4 ₂ /mnm
Lattice constant (nm)	a = 0.474 b = 0.319
Density (g cm ⁻³)	6.99
Melting point (°C)	>1900
Heat of formation (eV)	6.0
Band gap (eV)	3.6
Exciton binding energy (meV)	130
Electron mobility	100 – 200 cm ² V ⁻¹ S ⁻¹

2.3.3 Gas sensing mechanism of SnO₂ gas sensor

Generally, the metal oxide gas sensors can be categorised into bulk-sensitive materials and surface-sensitive materials. Bulk sensitive materials in particular titanium dioxide (TiO₂) increases conductivity due to bulk oxygen vacancies (Batzill and Diebold, 2005).

On the other hand, SnO₂ is also grouped in the surface sensitive materials although bulk defects affect their conductivity. The direct band gap and high electron mobility of surface-sensitive materials resulted in large variation in electric conductance even with a slight change in charge carrier concentration. Consequently,

the conduction band bending induces strong conductivity changes in sensor material and eventually trigger the gas response signal (Wu *et al.*, 2010).

The fundamental gas sensing mechanism of SnO₂ is based on the electrical conductivity changes experienced by an n-type semiconducting metal oxide. When the surface chemisorbed oxygen reacts with a reducing gas (e.g. CO, H₂, H₂S, CH₃OH, C₂H₅OH, etc.), the sensor resistance decreases, whereas the resistance increases with oxidising gas (e.g. O₂, NO₂, O₃, etc). In the case of a p-type semiconductor the effect on the sensor resistance is *vice versa*.

Typically, oxygen molecules from the air are adsorbed on the surface of the SnO₂ sensing material. It was stated the form of chemisorbed oxygen either atoms or molecule depends mainly on the operating temperature of the SnO₂ sensor (Barsan and Weimar, 2001). Based on the results obtained from FTIR, temperature programmed desorption (TPD) and electron paramagnetic resonance (EPR) spectroscopy, it was proven that the SnO₂ surface dominated by oxygen molecules at temperature below 150 °C, whereas ionic oxygen species dominates the SnO₂ sensor surface at higher temperature (Barsan and Weimar, 2001). The transfer of electrons from the SnO₂ sensor surface to the adsorbed oxygen molecules induced the bending of conduction band compared to the flat band. Figure 2.2 shows the schematic diagram of band bending near surface region of SnO₂ sensing material. A negative surface charged bends the bands upward, where the Fermi level was pushed into the band gap of SnO₂. Subsequently, it reduces the charge carrier concentration and resulting electron depletion region near the surface of the sensor particles. Electrons depletion leads a positive space charge region that compensates for the negative surface charge (Wang *et al.*, 2010).

The returning of electrons to the conductive band decreases the resistance (Korotcenkov, 2013). The schematic diagram of the gas sensing (reducing gas) mechanism on SnO₂ sensor surface is shown in Figure 2.3.

On the other hand, the reaction between oxidising gas and chemisorbed oxygen results in acceptance of electrons from the conduction band of the sensor (Equations 2.3 and 2.4). The capture of electrons during the reaction increases the resistance (Korotcenkov, 2013).



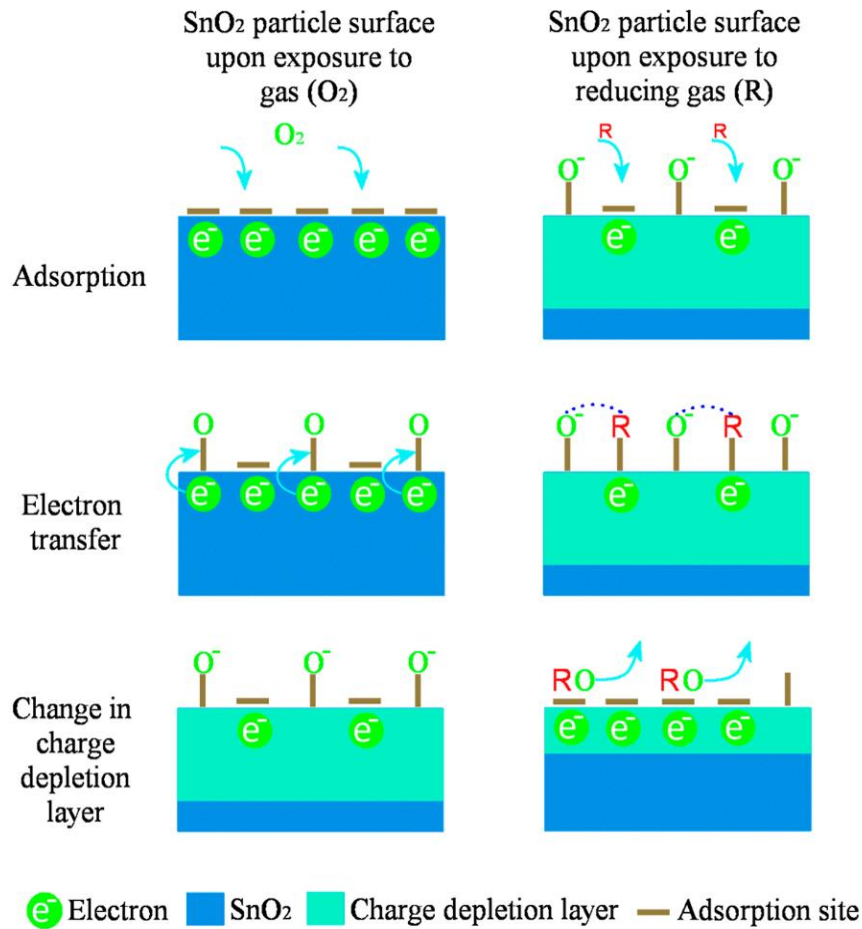


Figure 2.3: Schematic diagram of the reducing gas sensing mechanism on the SnO₂ surface (Tangirala *et al.*, 2017).

It is noteworthy that the pure SnO₂ sensor material surface has relatively less active sites available for oxygen adsorption compared to noble metals and transition metals, due to the formation of potential barriers on the particle surface (Liu *et al.*, 2014). Furthermore, it was found that in n-type semiconducting material such as SnO₂, electrons only contribute small fraction (<1%) to the total conductivity (Park and Akbar, 2003). Thus, two important efforts have been taken: firstly, reduce the size of SnO₂ particles to nano size scale and secondly, incorporating dopants which have relatively higher number of catalytic active sites compared to pure SnO₂. These two important efforts can have a significant impact on the SnO₂ sensor performance, as are discussed further in subsections 2.3.3(a) and 2.3.3 (b), respectively.

2.3.3(a) The effect of small grain size of SnO₂ sensor material

The effect of grain size of SnO₂ sensor material was explained by Xu and co-workers using a semi quantitative model (Xu *et al.*, 1991). According to this model, the SnO₂ particles are considered to be partially sintered crystallites which are connected to their neighbour particles by neck (Eranna, 2011) as shown in Figure 2.4. Figure 2.4 shows the schematic model of the effect of the crystallite size on the sensitivity of SnO₂ gas sensors. Basically, the relationship between the particle size (D) and the thickness of electron depletion layer (space-charge layer) around the particle surface may lead to three different phenomena. Firstly, when D is very much larger than L ($D \gg 2L$), the conductivity is effectively controlled by the inner mobile charge carriers and the electrical conductivity depends exponentially on the barrier height. At this state, the sensor material is not so sensitive to the charge acquired from surface reactions. Based on the literature review it was estimated that the size of L for pure SnO₂ material is about 3 nm (Ogawa *et al.*, 1982; Yin *et al.*, 2009; Zhang *et al.*, 2009). While when $D \geq 2L$, the space charge layer region around the neck forms a constricted conduction channel within each aggregate. Thus, the conductivity of the SnO₂ depends on the grain boundaries and the cross-section area of those channels. Therefore, the SnO₂ particles are sensitive to the oxygen gas in atmosphere.

Lastly, if the D is less than 2L ($D < 2L$), the space charge layer region occupies the entire SnO₂ particle and the crystallites and the conductivity is determined by charge transport in the bulk. At this stage, the energy bands are nearly flat throughout the whole structure of the interconnected grains and there is no significant barrier for intercrystallite charge transport. Thus, a few charges from surface reactions will result in substantial changes in conductivity of whole structure, consequently SnO₂ becomes highly sensitive to oxygen in atmosphere (Geng *et al.*, 2010).

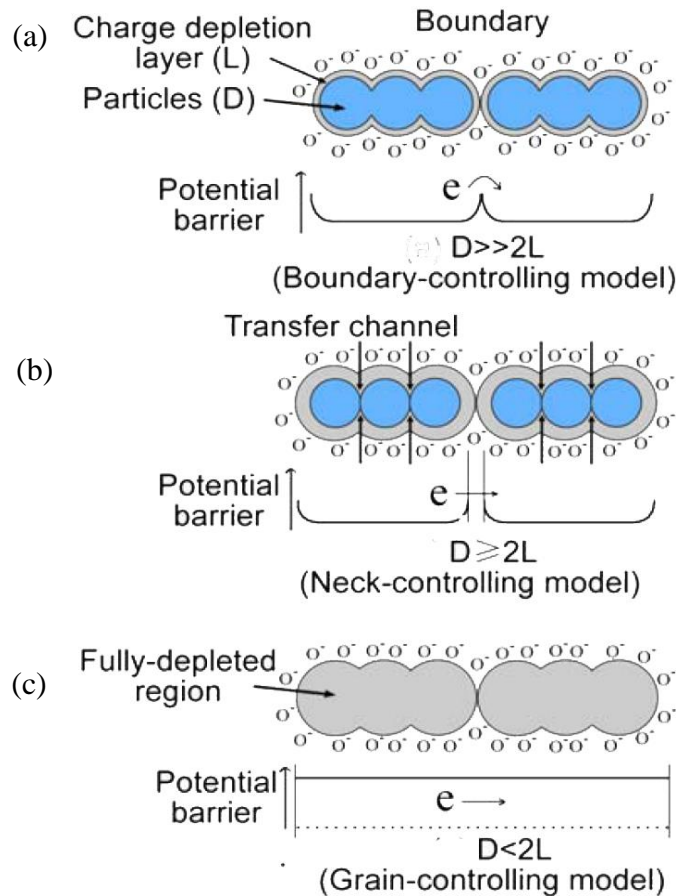


Figure 2.4: The schematic model of the effect of the crystallite size on the sensitivity of SnO₂ gas sensors: (a) Boundary-controlling model, (b) Neck controlling model and (c) Grain-controlling model (Sun *et al.*, 2012)

2.3.3(b) Mechanisms of gas sensing in metal doped SnO₂ nanostructures

Decreasing the size of SnO₂ particles to nanosize can significantly improve the gas sensing properties, achieving small dimensions remains as challenge in real applications. For example, the SnO₂ nanostructures with particle size less than 10 nm can have poor mechanical properties (Liu *et al.*, 2014). In addition, the size of SnO₂ crystallite can grow as the sensor is heat-treated to obtain good sensing properties during the gas sensing process, which can affect the performance of SnO₂ gas sensor (Miller *et al.*, 2006). Thus, doping is always considered as a traditional technology that can improve the physical and chemical properties of gas sensor (Lim and Oh, 1996; Liu *et al.*, 2011; Parthibavarman *et al.*, 2013; Jin *et al.*, 2015).

In general, the type of dopants may influence the gas sensing properties of SnO₂ mainly by inhibiting the grain growth and modifying the electron Debye length, eventually change the gas-surface interactions (Batzill and Diebold, 2005). Two different mechanisms are invoked to explain the sensitisation phenomenon of SnO₂ doped sensors: the electronic and the catalytic mechanisms. Figure 2.5 presents the schematic diagram of electronic and catalytic mechanisms in metal doped SnO₂ gas sensor. In the electronic mechanism, a reducing gas reacts on the surface of the metal dopant, releasing an electron that is transferred to SnO₂. The changes in the electron density near the surface of the SnO₂ leads to a decrease in resistance. In the catalytic mechanism which also known as spill-over mechanism, the metal dopant acts as a catalyst where the reducing gas is transported to the SnO₂ surface. When the reducing gas reacts with oxygen adsorbed on SnO₂ surface, the electrons release directly to the charge depletion layer of SnO₂ particle. The difference between these both mechanisms is that electrons transfer occurs in electronic mechanism, while atoms transfer occurs in the catalytic mechanism (Miller *et al.*, 2006).

Another role of doping in enhancing gas sensing properties is that by reducing the particle size SnO₂. This phenomenon was explained by Wu and co-workers (1999), due to the interaction on the boundaries between the host and dopant crystallites, the motion of crystallites is resisted, and the crystal growth stunted. As the result, the particle size is decreased by the metal doping (Wu *et al.*, 1999).

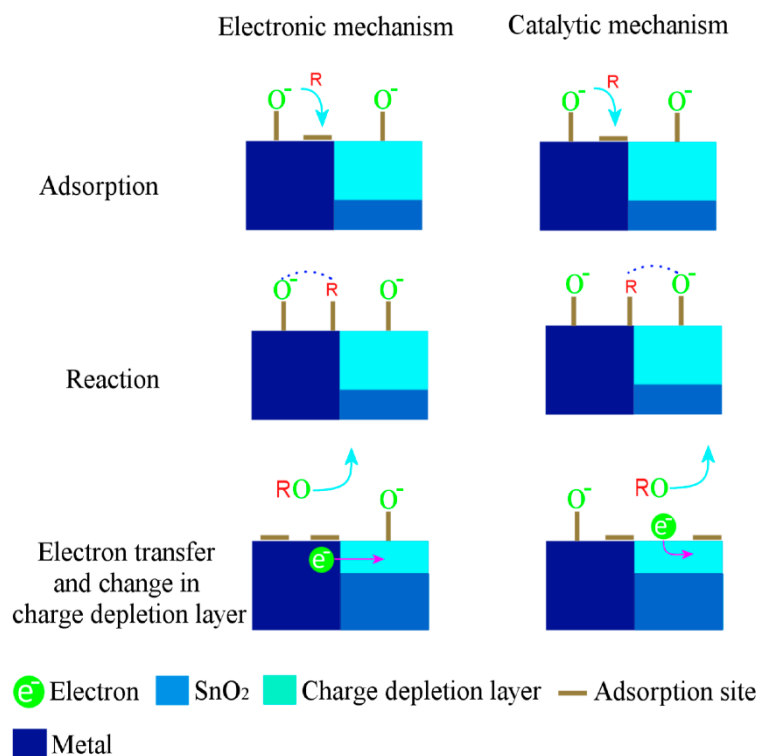


Figure 2.5: Schematic diagram of the electronic and catalytic mechanisms in metal doped SnO₂. R represents reducing gas (Tangirala *et al.*, 2017).

2.3.4 Metal additives (dopants) in SnO₂ gas sensors

The doping of tin(IV) oxide gas sensor is one of the traditional approaches used to enhance the gas sensitivity, selectivity and decrease the operating temperature. So far, various dopants including noble metals, transition metals, non-metals, alkaline earth metals and metalloid can be used. Among them, noble metals (Pd, Pt, Au, Ag, Rh) and transition metals (e.g. Fe, Co, Cu, Ni, etc.) are the most common metals used as dopants in gas sensor applications. Generally, noble metal dopants serve as “catalyst” (increase the rate of reaction) whereas transition metal dopants serve as “accelerator” (its presence cause an increase in the speed of chemical reaction) of various process (Korotchenkov, 2013). Doping can be categorised as bulk doping and surface doping. The bulk doping is normally carried out during the synthesis process of SnO₂, while surface doping can be performed following sensing layer deposition.